Applied Thermal Engineering 236 (2024) 121517

Contents lists available at ScienceDirect

Applied Thermal Engineering

journal homepage: www.elsevier.com/locate/apthermeng

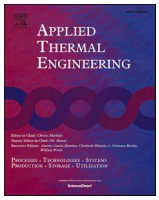

Research Paper

The energy performances of an elastocaloric device for air conditioning through numerical investigation

Luca Cirillo *, Adriana Greco, Claudia Masselli

Dipartimento di Ingegneria Industriale - Università degli Studi di Napoli Federico II -Piazzale Tecchio 80, 80125 Napoli, Italy

ARTICLE INFO

Keywords:
Elastocaloric effect
Rotary model
Multiphysics simulations
Thermo-fluidodynamic model
Energy performances

ABSTRACT

The urgent needing to address global warming and the rapid depletion of fossil fuel reserves has led to a demand for immediate research in sustainable and clean energy technologies. Elastocaloric cooling is a promising proposal for clean refrigeration because of the zero global warming potential of the shape memory alloys, which are solid-state materials showing elastocaloric effect. The latter manifests when the shape memory alloys are stressed through a mechanical loading, transforming from the austenite phase toward the martensite one and releasing heat, dually transforming from the martensite phase into the austenite phase and absorbing heat. The updated literature accounts for 15 elastocaloric cooling devices, but none is close to commercialization. The efforts are devoted to making this decisive step by implementing new efficient devices.

This paper analyses the energy performances of an elastocaloric rotary prototype employing binary NiTi wires through the first rotary bidimensional numerical model based on the finite element method to attain the device's potential cooling and heating capacities. In this paper, the energy performances of an elastocaloric rotary prototype employing binary NiTi wires are analyzed through a 2D numerical model based on the finite element method to attain the device's potential cooling and heating capacities. The model reproduces the thermo-fluid-dynamic behaviour of an experimental rotary device for air conditioning; meanwhile, the secondary fluid in the device is air. The accuracy of the rotary model easily allows to optimize the operating parameters of the elastocaloric prototype under construction.

Results in terms of outlet air temperature, cooling power and coefficient of performance are presented for different air velocities inside the air channel and different rotation frequencies of the device. A performance map has been obtained by exploring the device's behaviour in the cooling mode under variable working conditions to identify the optimal configuration. A maximum COP of 6.22 (corresponding to a second law analysis efficiency of 60%) was evaluated under an airflow speed of 6 m s^{-1} and a frequency of 0.3 Hz, corresponding to $\phi^* = 0.44$. 28.5 K and 5400 W kg^{-1} are the reached peaks of temperature span and cooling power.

1. Introduction

1.1. Background and general views

Refrigeration and air conditioning are fundamental pillars of modern society. The consumption associated with this sector grows exponentially in both developing and developed countries. In developed countries, the use of environmental conditioning is now widespread. Therefore, refrigeration and air conditioning play an important role in overall energy consumption and, consequently, in CO_2 emissions. This quota represents about 20% of global energy consumption in developed countries.

The problem is not only related to energy consumption: all traditional systems are based on vapor compression, over a century-old technology. Therefore, although the energy efficiency of this technology has increased over the years, it is still less than 30–40% of the Carnot Coefficient Of Performance (COP). No further improvements in this value are planned because vapor compression has reached its technological limits. Another ecological problem of this technology is related to refrigerants, which have presented various environmental problems over the years. Since 1987, when the Montreal Protocol [1] was signed, until today, the global refrigeration and air conditioning industry has made big progress in addressing the twin environmental threat of ozone depletion and climate change. This treaty triggered a technological revolution, and since then, the refrigeration and air conditioning

* Corresponding author.
E-mail address: luca.cirillo2@unina.it (L. Cirillo).

https://doi.org/10.1016/j.applthermaleng.2023.121517
Received 30 March 2023; Received in revised form 28 August 2023; Accepted 5 September 2023
Available online 7 September 2023

Nomenclature

Roman symbols

A	Austenite phase temperature, K
B	Boltzmann constant, m^2 kg s^{-2} K^{-1}
C	coefficient of K-$\widehat{\varepsilon}$ model
c	specific heat capacity, J kg^{-1} K^{-1}
COP	Coefficient Of Performance, -
D	diameter, mm
E	energy, MPa
$\bar{E}$	Young modulus, MPa
f	frequency, Hz
g'''	elastocaloric term, W/m^{-3}(−|-)
H	Latent heat, J/g
h	convective heat transfer coefficient, W m^{-2} K^{-1}
$\vec{\bar{I}}$	identity vector, -
K	turbulent kinetic energy, J
k	thermal conductivity, W/m K^{-1}
L	length of the wire, mm
M	Martensite phase temperature, K
m	Mass, kg
$\dot{m}$	flow rate, kg s^{-1}
n	number of times
Nu	Nusselt number, -
p	pressure, Pa
Pr	Prandtl number, -
$\dot{Q}$	thermal power, W
Re	Reynolds number, -
s	entropy, J kg^{-1} K^{-1}
T	temperature, K
t	time, s
u	x-velocity field component, m/s
$\bar{u}$	Velocity vector, m/s
V	volume, m^3
v	y-velocity field component, m/s
$\dot{W}$	mechanical power, W
w	loading/unloading work, J/g
x	longitudinal spatial coordinate, m
y	orthogonal spatial coordinate, m

Greek symbols

Δ	finite difference
ε	strain, N
$\widehat{\varepsilon}$	turbulent cinematic viscosity, m^2 s^{-1}
μ	dynamic viscosity, Pa/s
μ_T	turbulent dynamic viscosity, Pa/s
η	efficiency
θ	period, s
υ	cinematic viscosity, m^2/s
ξ	phase fraction, -
$\dot{\xi}$	instantaneous phase fraction, s^{-1}
ρ	density, kg m^{-3}
σ	uniaxial stress, MPa
τ	convective heat exchange transient constant, s
ψ	probability, -
Φ*	utilization factor, -

Subscripts

0	Initial
1	final
A	Austenitic
AM	Austenite-to-Martensite transformation
ad	adiabatic
air	air
Carnot	Carnot ideal inverse cycle
cycle	cycle
cold	cold regenerator
eff	effective
env	environment
f	finish
hot	hot regenerator
inlet	Inlet
K	Kinetic Energy
load	Loading
m	Mean
M	Martensitic
MA	Martensite-to-Austenite transformation
MAX	maximum
mech	mechanical
net	net
outlet	Outlet
p	constant pressure
pump	pump
ref	refrigeration/cooling
s	Start
SMA	Shape Memory Alloy
span	span
T	constant temperature
unload	unloading
wire	single wire
x	along x-coordinate
y	along y-coordinate
II	second law of thermodynamic

industry has developed several generations of alternative fluids to replace ChloroFluoroCarbons (CFCs), including transient Hydro-ChloroFluoroCarbons (HCFCs), which are now being phased out in developed countries and those that include HydroFluoroCarbons (HFCs) due to high Global Warming Potential (GWP) [2,3]. Due to regulations deriving from the Kyoto Protocol [4], high-GWP HFC refrigerants are being replaced in developed countries [5]. So the only acceptable solutions for contributing to the direct greenhouse effect are refrigerant fluids with low or zero GWP (such as natural fluids) [6]. However, the new generation of refrigerants with low GWP presents several problems related to availability, high cost, lower energy performance, and flammability. Therefore, the problem of developing eco-friendly refrigerants is still open in developed countries while developing countries continue to use refrigerants polluting both for high GWP and for non-zero Ozone Depletion Potential (ODP) values, i.e. HCFC [7].

From what has been said, the need to develop new refrigeration techniques alternative to eco-sustainable vapour compression arises. Among the Not-in-Kind refrigeration technologies, particular importance is devoted to those based on solid-state refrigerants manifesting a caloric effect [8]. The caloric effect that some materials can present is related to the variation of an external field that can be a magnetic, electric, tensional or pressure field from which magneto-, electro-, elasto- or baro- caloric refrigeration derives [9].

Caloric refrigeration is a promising proposal for clean refrigeration because of the zero global warming potential of the caloric materials that are solid state, which reflects on no direct contribution to the greenhouse effect. Magnetocaloric is the first technique that was paid attention to by the scientific community since the beginning of 1970

[10–15]. Around the world, more than 100 prototypes have been developed in various research laboratories [16]. However, this technology has never been able to be attractive from a commercial point of view for various reasons: it elevates economic expenditure and encumbrance of the apparatus engendering magnetic; elevates economic expenditure for the magnetocaloric materials (most of them are rare earth family of the periodic table), not fully encouraging temperature spans and powers, as well as coefficient of performance. Elastocaloric seems to represent a good proposal: solid refrigerants widely available on the market and with low-cost, easy-to-find mechanical drivers to exert the mechanical stress, high-temperature spans. The elastoCaloric effect (eCE) can be detected in a temperature fluctuation deriving from mechanical stress imposed on an elastocaloric material. Shape Memory Alloys (SMA) are materials provided by eCE with the property of remembering their geometrical form owning before applying the stress and being able to come back in again [17–20].

The eCE can be used in a cycle based on an Active elastocaloric Regenerative refrigeration (AeR) cycle to produce a refrigeration effect (Discussed in the Supplementary Material in the section "The cycles based on the elastocaloric effect"). In an AeR the SMA works both as a solid refrigerant and regenerative medium.

1.2. State of the art

To report an accurate state of the art of developed devices based on eCE, they can be divided as: i) the ones based on conductive (solid to solid) heat transfer typical of small-size devices [21]; ii) the ones where the heat transfers are regulated by convection between the elastoCaloric material (eCM) and a transport fluid. The latter group embraces devices that can be extended to the macro-scale size and that are typically based on the AeR cycle. The loading mechanism of these devices can be tension or compression.

In this state-of-the-art, the focus is on the prototypes belonging to the second group as we want to develop a device that can work on the macro-scale.

In 2012 a beginner elastocaloric cooler was proposed [22]. The prototype was rotary, based on the tension of small diameter NiTi wires (0.5 mm), and it uses air as a secondary fluid. The experimental data are very few, except for the temperature span of 17 K under a strain of 8.5%. The main problems were both related to the mechanical friction in the wire loading phase and to the short fatigue life of the wires.

The first compression prototype was presented by Qian et al. in 2015 [23]. The prototype consists of two active regenerators made with NiTi binary alloy tubes with compression work recovery. Two servo motors drive a linear actuator to compress the two beds. The auxiliary fluid used is water, and 1.5 K is the greatest temperature span (ΔT_{span}); a maximum cooling power of 38 W was achieved. Subsequently, modifications were made to the same device to improve its performance through an optimization algorithm [24], which allowed exploring the prototype's potential and obtaining a maximum theoretical COP of 4.1.

The same research group [25] has developed a second-generation prototype composed of four regenerators, each of them containing 37 symmetrically arranged NiTi tubes. The drivers used to compress the tubes were hydraulic cylinders, with water as the secondary fluid. No experimental results of this prototype are available in the literature; results obtained with a dynamic model of 11 as COP and 24.6 K as temperature span have been provided.

The device described in [26] has the elastocaloric material with the shape of 9 thin plates (200 μm thick) of $Ni_{55.8}Ti_{44.2}$ subjected to a tension force through a linear actuator. The secondary fluid used is water. The performances of the device have been studied in detail for different deformations. 15.3 K of temperature drop, 0.784 W g^{-1} specific power and a COP of 3.5 were reached at 3.4% strain. At lower strain, the device achieves a COP of 5.5, with a temperature span of 6.5 °C and power of 0.355 W g^{-1}. In a second set of experiments [27] with a slightly improved device configuration, a maximum no-load temperature range of 19.9 K with a strain of 3.5% was achieved, but no more than 6000 cycles were achievable.

In 2018 Kirsch et al. [28] introduced a rotary device tension-based with air as an auxiliary fluid. The elastocaloric material has the shape of thin wires (0.2 mm) of the quaternary alloy $Ti_{55.2}Ni_{29.3}$ $Cu_{12.7}Co_{2.8}$. The device takes up the idea of Saylor of 2012 [22]; however, for loading, it uses a camshaft that transforms the rotary movement into a linear stroke. During the simulation tests, the device reaches a ΔT_{span} of 6 K with an airflow rate of 46 m^3/h. If the airflow is increased to 133 m^3/h, there is a decrease in the ΔT_{span} (5.1 K). With a strain of 4.7%, a COP of 9.5 and a cooling power of 250 W at a frequency of f = 0.5 Hz were found.

Cheng and Sun [29] presented a compact bending-based NiTi elastocaloric air cooler. The elastocaloric material is $Ni_{56}Ti_{44}$ and has the shape of a thin plate (thickness of 0.50 mm, width of 25 mm and length of 100 mm). The plates are mechanically flexural loaded via a linear actuator. The experimental results showed that with deformation of 7.20%, the specific load required is 5.64 N g^{-1}, two orders of magnitude less than compressive or tensile load. Analyzing a single plate, the ΔT_{span} was 5.5 K with a specific cooling power of 0.137 W g^{-1}. A device with several plates reached a cooling power of 11.5 W.

Ianniciello et al. [30] constructed and tested an elastocaloric device capable of overcoming one of the major drawbacks of elastocaloric devices: the reduced duration of the eCM. This elastocaloric regenerative cooling system operates in compression. The regenerator consists of eight $Ni_{56.2}Ti_{43.75}$ tubes arranged in a crossflow configuration with a height of 9 mm. The regenerator housing has a round base (1.76 mm internal and 2.40 mm external diameters) with two thick metal plates on the outside to resist compressive force. The secondary fluid is water, and a linear actuator is used for circulation. The device exhibited a very long fatigue life, able to resist to more than 100.000 cycles without failure. With a cooling power of 1.5 W, i.e. 1071 W kg^{-1} a temperature of 0.4 K was measured for an active material mass of only 1.4 g, and 5 K is the greatest ΔT_{span}.

A new conception of elastocaloric prototype has been developed by Ahcin et al. [31] based on a shell and tube regenerator made of a binary alloy NiTi (55.92 %wt Ni). The device is based on compression, and the secondary fluid is water. The 18 tubes of NiTi have an outer diameter of 3.0 mm and an inner of 2.5 mm, with a total mass of 13.7 g. The device is a heat pump; the experimental results show 31.3 K as the temperature span, a maximum heating power of 60 W, corresponding to a specific power of 4.4 W g^{-1} with a COP of 5.8.

The latest introduced elastocaloric device in scientific literature is the one of Qian et al [32] based on the compression of NiTi tubes and able to achieve a maximum temperature span of 22.5 K and a cooling power of 260 W.

Crucial for constructing an experimental prototype is the development of numerical models able to reproduce the device's behaviour. Several models in the open literature are mostly one-dimensional and, therefore, suitable for modelling an alternative prototype [33–36].

1.3. The research gap and the goal of the paper

Based on the state of the art presented, the following considerations can be drawn: i) there are no experimental results on prototypes based on the macro-scale, although some have been developed; ii) to solve the problem of the short fatigue life of elastocaloric materials the scientific community moves in the direction of developing prototypes based on compression. However, these prototypes have been developed only for small-size devices, and it appears difficult to scale the size; iii) all the devices presented show very poor energy performances and are always lower than those of traditional vapor compression plants; iv) there are no two-dimensional (2D) or three-dimensional (3D) models that can be used to simulate a rotating device; v) a sensitivity analysis to understand the functioning of a real device under different operative conditions has not been conducted.

This work aims to design an elastocaloric prototype for an application in the macro-scale field. The idea of this prototype stems from the need to find an eco-compatible solution for the air conditioning sector [37]. The device is a continuous flowing air conditioner based on rotation. To correctly design and optimize the prototype a 2D numerical model has been developed. The model is able to simulate the real rotation of the device and the resulting fluid dynamic effects. In this paper, a numerical investigation of the design of the experimental prototype is presented. The goal of the paper is to present a complete map of the energy performance of the device varying the operative conditions in order to understand its potential.

The newness of this work is translatable in: i) the project of an elastocaloric prototype for macro-scale applications; ii) the development of a 2D rotary model for the design of the device; iii) the structuring of a performance map by varying the operating conditions.

2. Developing the experimental prototype

The experimental prototype under construction is designed for environmental conditioning; air is the auxiliary fluid so to avoid the employment of intermediate heat exchangers. The rotary design of the device continuously flows through hot and cold air. The elastocaloric material is shaped as 600 wires (diameter 0.5 mm and length 300 mm) arranged in the annular section between two concentric cylinders (internal radius of 120 mm, an external radius of 135 mm, and a length of 300 mm). The annular section is divided into two channels: hot and cold. Figs. 1 and 2 show 3D diagrams of the device. In Fig. 1 also the placement of the air inlet and outlet channels are clearly schematized and underlined.

The prototype is based on loading through tensile mechanism ensured by 10 hydraulic pistons, each one connected to a bunch grouping 60 wires. Hydraulic pistons ensure friction over previous prototypes based on a cam track [28] or on the inclination angle of one of the disks [22]. The rotating axis is connected to the rotating disks. Ball bearings are used to prevent friction during the rotation of the disk.

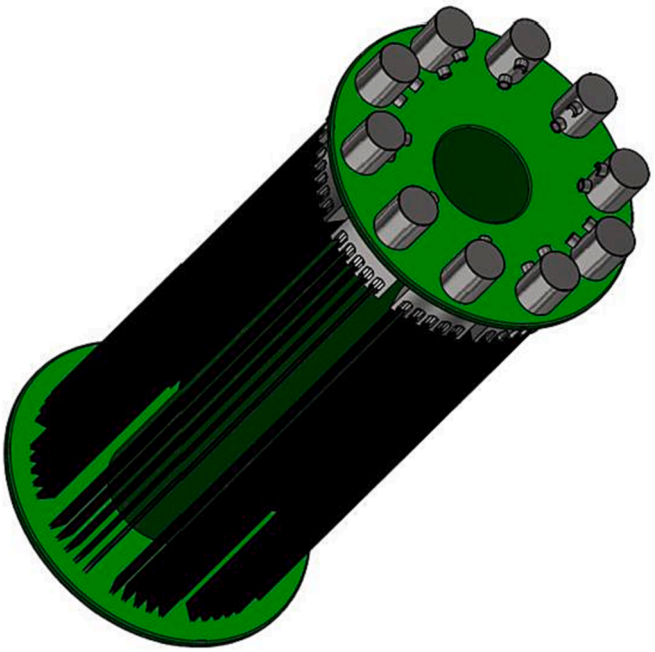

Fig. 2. A schematic view of the interior part of the experimental device.

During the rotation of the disks, always half of the circumference is characterized by loaded wires. To prevent the deflection of the disk, thrust ball bearings are installed. It was necessary to use a coupling system with epicyclic gears that allowed for disconnection from the "central" stator axis and the rotating disks.

The pistons are connected in groups of two to ensure work recovery. The application/remotion of the stress to the wires takes place in the two transition zones located between the air inlet and outlet channels. In the

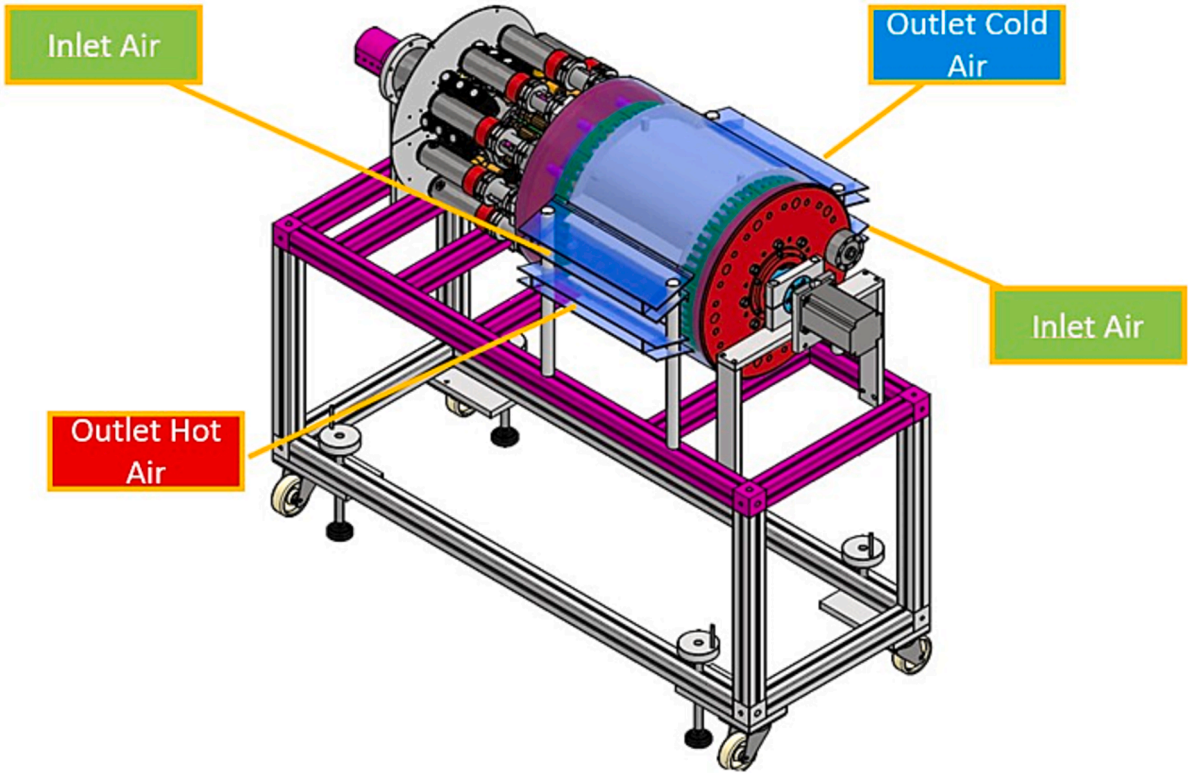

Fig. 1. A schematic view of the exterior part of the experimental device.

prototype, the internal and external cylinders are fixed, as well as the conveyors, while rotating are the pistons and the wires of elastocaloric material. The system rotates synchronously by rotating the tambour, including the inner casing.

The loading apparatus of the elastocaloric wires is high-pressure hydraulically-based consisting of:

- a self-priming high-pressure electro-pump with a flow rate of 90 L min^{-1} and 200 bar as maximum pressure;
- a primary oil tank on which the pump is placed, complete with filters, a safety solenoid valve, and a maximum pressure regulator of 200 bar;
- two secondary accumulators, one to stabilize the high-pressure output and the other in the medium-pressure "common rail" line for work recovery.
- three high-pressure solenoid valves per each hydraulic cylinder that supply power to the 24 V (DC) solenoids.

The hydraulic actuator is connected to the mechanism (plug and threaded rings) clamping the wires through an extension shaft. The central shaft (the stator) with suitable machining to accommodate the ball bearings, sized to support the rotation of the rotating system and various traction components.

The inner and outer cylinders define the channel where air can flow. Three radial fans are fixed to the inlet conveyor to provide a maximum airflow of 620 m^3/h. A coaxial support is fixed on the central shaft, which is necessary for securing the internal conveyor.

The need to rotate the entire system, including the actuators, necessitated studying a solution that would allow for transferring hydraulic oil from a fixed part to a rotating part of the machine. The solution adopted was the use of a hydraulic rotating oil coupling. This type of coupling allows for connecting multiple hydraulic elements equal to the number of available ports. In our case, connecting 30 solenoid valves, 3 for each of the 10 actuators used for the traction/relaxation of the Nickel-Titanium shape memory wires is necessary. The need for 3 solenoid valves for each actuator is related to the operation of the hydraulic system. This operation requires the use of hydraulic oil at three different pressures: the high-pressure hydraulic pump group pressure (adjustable up to 200 bar) from the first accumulator, the medium pressure (estimated at approximately 50 bar) from the second accumulator, and a third pressure relief line. In terms of diagnostics and controls, an angular position transducer (optical encoder) will also be installed, which is necessary for managing the sequence and logic of operation.

The rotational motion of the system results in a mixing of hot and cold air in the intermediate zone between the cooling and heating sections of the microfilaments. To overcome this issue, it has been proposed to insert obstacles between the air inlet and the outlet. These flexible material obstacles are attached to both the internal and external conveyors. As they are made of flexible material, the obstacles allow the passage of wires during rotation while providing resistance to the airflow, thus limiting the mixing of ambient temperature air with the heated or cooled air.

The prototype thus designed mounts a mass of solid-state refrigerant of 230 g, and therefore it ensures a maximum cooling power of around 1 kW but is scalable because an increasing number of wires results in an augmentation of the cooling capacity.

3. The 2D rotative numerical model

To correctly design the experimental device, optimizing the geometric parameters (height of the channel, transition zones, distance between the wires) and the operating ones (air speed and rotation frequency) is necessary. To this aim, a 2D rotary model has been developed, which is able to provide the velocity, temperature and pressure field of the air and the temperature field of the SMA. Furthermore, the model takes into account the elastocaloric effect produced by NiTi wires as discussed in the Supplementary Material Section "The elastocaloric effect and materials".

The simplifying assumptions used in the model are the following: 1) the air is considered incompressible and with constant properties; 2) the SMA is considered to have constant properties; 3) the radiation term is neglected; 4) the regenerator is considered to be adiabatic toward the outside environment; 5) the viscous dissipation function has been neglected in the air energy equation.

In this paper, the geometric parameters have been fixed, whereas the operating ones have been optimized to explore the potential of the device in terms of energy performance and, therefore, to build operating maps.

Given the axial symmetry, Fig. 3 shows a section of the device. The Figure shows the wires of elastocaloric material characterized by a longitudinal pitch equal to 2.5 mm and a transversal pitch of 5.5 mm. The inclination of the device's air inlet and outlet channels results from a fluid-dynamic optimization to promote contact between air and elastocaloric wires.

In the transition zones, the application/remotion of the stress to the wires takes place in a time of 0.2 s to consider the transformation as adiabatic.

Obstacles have been placed in the transition areas to avoid unwanted mixing of hot and cold air (i.e. hot air leaving the warm regenerator with air at room temperature entering the cold regenerator on the left, or cold air leaving the cold regenerator with air at room temperature at the inlet of the hot regenerator on the right). Turbulence promoters have been placed in the inner and outer cylinders to improve the heat exchange. The air motion within the channel is turbulent for the tested velocity values. The equations governing the system are:

- air mass continuity equation:

$$\frac{\partial \rho}{\partial t} + \nabla(\rho \overline{u}) = 0 \tag{1}$$

- air momentum equation:

$$\rho \frac{\delta \overline{u}}{\delta t} + \rho(\overline{u} \bullet \nabla)\overline{u} = \nabla \bullet \left\{ -p\overline{I} + (\mu + \mu_T)\left[\nabla \overline{u} + (\nabla \overline{u})^T\right] \right\} \tag{2}$$

where μ_T represents the turbulent flow viscosity defined as:

$$\mu_T = \rho C_\mu \frac{K}{\widehat{\varepsilon}} \tag{3}$$

where C_μ is a constant of K-ε model for turbulent flow.

- Air energy equation:

$$\frac{\partial \rho E}{\partial t} + \nabla \bullet \left[\overline{u}(\rho E + p)\right] = \nabla \bullet \left[k_{eff} \nabla T + \tau_{eff} \bullet \overline{u}\right] \tag{4}$$

where k_{eff} represents the effective conductivity that is the sum of air (k_{ari}) and the turbulent flow (k_T) conductivity.

The turbulent flow kinetic energy is evaluated with the K-$\widehat{\varepsilon}$ model as:

$$\frac{\partial(\rho K)}{\partial t} + \rho \overline{u} \bullet \nabla K = \nabla \bullet \left[\left(\mu + \frac{\mu_T}{\sigma_K}\right)\nabla K\right] + p_K - \rho \widehat{\varepsilon} \tag{5}$$

where p_K can be evaluated as:

$$p_K = \mu_T \left[\nabla \overline{u} : \left(\nabla \overline{u} + (\nabla \overline{u})^T\right) - \frac{2}{3}(\nabla \bullet \overline{u})^2\right] - \frac{2}{3}\rho K \nabla \bullet \overline{u} \tag{6}$$

$$\frac{\partial(\rho \widehat{\varepsilon})}{\partial t} + \rho \overline{u} \bullet \nabla \widehat{\varepsilon} = \nabla \bullet \left[\left(\mu + \frac{\mu_T}{\sigma_{\hat{\varepsilon}}}\right)\nabla \widehat{\varepsilon}\right] + C_{\hat{\varepsilon}1} \frac{\widehat{\varepsilon}}{K} p_K - C_{\hat{\varepsilon}2} \rho \frac{\widehat{\varepsilon}^2}{K} \tag{7}$$

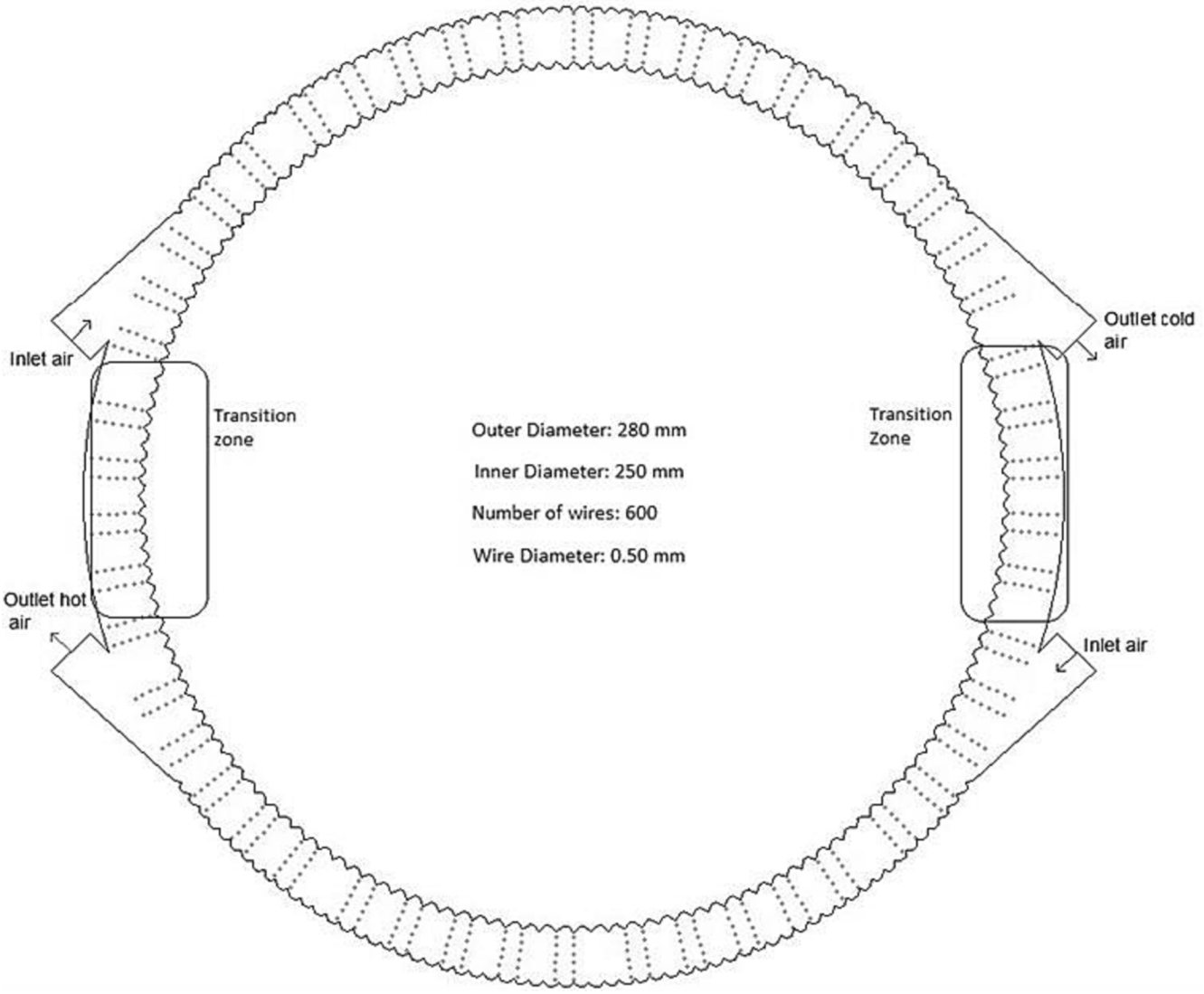

Fig. 3. A 2D axial section of the device.

The values of the constants for the K-$\widehat{\varepsilon}$ model are reported in Table 1.

- SMA energy equation:

$$\frac{\partial T_{SMA}}{\partial t} = \frac{k_{SMA}}{\rho_{SMA} C_{SMA,p}} \left(\frac{\partial^2 T_{SMA}}{\partial x^2} + \frac{\partial^2 T_{SMA}}{\partial y^2} \right) + g''' \tag{8}$$

during loading and negative during unloading. This term can be evaluated with the following equation:

$$g''' = \rho_{SMA} (\Delta H + w) \dot{\xi}_M \tag{9}$$

where w is the net work required:

$$w_{net} = w_{load} - w_{unload} \tag{10}$$

Table 1
K-$\widehat{\varepsilon}$ model coefficients.

Constant	Value
C_μ	0.09
$C_{\widehat{\varepsilon}\,1}$	1.44
$C_{\widehat{\varepsilon}\,2}$	1.92
σ_k	1.0
σ_ε	1.3

This work can be seen as the area confined in the hysteresis cycle of the SMA.

Where $\dot{\xi}_M$ can be valued through the differential equation:

$$\dot{\xi}_M = -\xi_M \psi^{MA}(T_{SMA}, \sigma) + \xi_A \psi^{AM}(T_{SMA}, \sigma) \tag{11}$$

where:

$$\xi_M + \xi_A = 1 \tag{12}$$

The transition probabilities can be quantified based on the kinetic model of the single crystal [38]:

$$\psi^{AM}(T_{SMA}, \sigma) = \frac{1}{\theta} \frac{\exp\left(-a \left(\frac{\sigma_{AM}(T_{SMA}) - \sigma}{\bar{E}_A} \right)^2 \right)}{\mathrm{erf}\left(\sqrt{a} \ \frac{\sigma_{AM}(T_{SMA}) - \sigma}{\bar{E}_A} \right) + \mathrm{erf}\left(\sqrt{a} \ \frac{\sigma_{AM}(T_{SMA}) + \sigma}{\bar{E}_A} \right)} \tag{13}$$

$$\psi^{MA}(T_{SMA}, \sigma) = \frac{1}{\theta} \frac{\exp\left(-b \left(\frac{\sigma_{MA}(T_{SMA}) - \sigma}{\bar{E}_M} \right)^2 \right)}{\mathrm{erfc}\left(\sqrt{b} \ \frac{\sigma_{MA}(T_{SMA}) - \sigma}{\bar{E}_M} \right)} \tag{14}$$

where a and b can be defined as:

$$a = \frac{\overline{E}_A V_{SMA}}{2BT_{SMA}} \tag{15}$$

$$b = \frac{\overline{E}_M V_{SMA}}{2BT_{SMA}} \tag{16}$$

In these equations, the air temperature and the velocity at the device inlet have been assigned.

In the model, the binary alloy $Ni_{55.92}Ti_{44.08}$ was considered as the elastocaloric material, with air as auxiliary fluid at a fixed ambient temperature of 293 K. The stress is applied/removed in a time of 0.2 s (with ε 0.25 s^{-1}), so the transformation can be considered adiabatic.

In the simulations, the operating conditions were optimized regarding the air velocity at the device inlet and the rotation frequency.

The air velocity was varied in the interval:

$$v \in \{3.0; 6.0; 9.0; 12; 15; 18; 20\} \tag{17}$$

The rotation frequency is related to the fluid passage time and loading and unloading times. In these simulations, the fluid passage time was varied. The maximum cycle frequency was evaluated for each fluid velocity considering the time that the air takes to exchange heat with the wires. This time is correlated with the time constant τ (typically 3–4 τ):

$$\tau = \frac{\rho_{SMA} c_{SMA} V_{wire}}{hA_{wire}} \tag{18}$$

where the convective coefficient of air was evaluated through the Whitaker correlation [39]:

$$Nu = \frac{hD_{wire}}{k} = \left(0.40Re^{0.5} + 0.06Re^{0.67}\right)Pr^{0.4} \tag{19}$$

The cycle frequency was varied in the interval:

$$f \in \{0.30; 0.40; 0.50; 0.60; 0.70\} \tag{20}$$

As suggested by Tomc et al. [13], the utilization factor Φ* is an important term to obtain a comparison with another caloric refrigeration device, defined by:

$$\Phi^* = \frac{\dot{m}_f c_f t_f}{m_s c_s} \tag{21}$$

where $\dot{m}_f$ and c_f is the mass flow rate and the heat capacity of the air, respectively; m_s and c_s is the mass and heat capacity of the elastocaloric material, respectively; t_f Is the time for fluid to flow in the channel.

With the temperature values obtained in the simulations, the prototype can be characterized in terms of:

- Temperature variation in the cold regenerator:

$$\Delta T_{cold} = \left(T_{air,in} - \frac{1}{t_{cycle}} \int_{0+nt_{cycle}}^{t_{cycle}+nt_{cycle}} T_{air,outlet}(t)dt\right) \tag{22}$$

- temperature span:

$$\Delta T_{span} = \frac{1}{t_{cycle}} \int_{0+nt_{cycle}}^{t_{cycle}+nt_{cycle}} \left(T_{air,out,HR} - T_{air,out,CR}\right)dt \tag{23}$$

- cooling power:

$$\dot{Q}_{ref} = \frac{1}{t_{cycle}} \int_{0+nt_{cycle}}^{t_{cycle}+nt_{cycle}} \dot{m}_{air} c_{air} \left(T_{air,in} - T_{air,outlet}(t)\right)dt \tag{24}$$

- Coefficient Of Performance (COP):

$$COP = \frac{\dot{Q}_{ref}}{\dot{W}} \tag{25}$$

The input power gives the contribution $\dot{W}$ is the sum of the mechanical power per unit of time-related to the loading of the wires, the mechanical power required for the air motion (according to the pressure losses) and the contribution to the device's rotation, defined as:

$$\dot{W} = \dot{W}_{fan} + \dot{W}_{load} + \dot{W}_{rot} \tag{26}$$

where:

$$\dot{W}_{fan} = \frac{\dot{V}^*(\Delta p_{hot} + \Delta p_{cold})}{\eta_{fan}} \tag{27}$$

assuming a η_{fan} of 80%

$$\dot{W}_{load} = n_{wire}{}^*(F_{wire}{}^*\Delta z)^* f^* x_{rec} \tag{28}$$

$$\dot{W}_{rot} = 2\pi f^* M_t \tag{29}$$

$\dot{W}_{rot}$ is proportional to driving torque, i.e. also to the number of engine rpm and it is has been evaluated as neglectable with respect to the other components since very small is the number of rpm of the device (maximim is 18 per minute).

- Second law efficiency:

$$\eta_{II} = \frac{COP}{COP_{Carnot}} \tag{30}$$

This efficiency takes into account the COP of the device in cooling with respect to the maximum COP achievable that can be evaluated as:

$$COP_{Carnot} = \frac{T_{m,air,outcold}}{T_{m,air,outhot} - T_{m,air,outcold}} \tag{31}$$

where $T_{m,air,outcold}$ is the average value of the air temperature at the outlet of the cold regenerator and $T_{m,air,outhot}$ is the mean value of the air temperature at the outlet of the hot regenerator.

4. Grid independence and model validation

The model reported in equations (1)-(9) is solved through the finite element method through commercial software. A convergence criterion of the simulations based on a tolerance of x and y has been assumed as 1 × 10^{-3} and 5 × 10^{-5} with respect to the components of air velocity and temperature. The domain was subdivided using free triangular meshing with the following quality parameters: skewness average value equal to 0.55; a value of non-squareness equal to 53. Since the model is rotary, it was chosen to use a mobile mesh to accurately replicate the fluid dynamic and thermal behaviours associated with the rotation of the elastocaloric material.

The independence of the mesh was studied, and three different meshes were hypothesized (A, B, C), consisting respectively of 175000, 351,134 and 702,000 triangular elements. Table 2 shows the results obtained with the different meshes in terms of air temperature at the outlet of the cold regenerator with an inlet speed of 9 m s^{-1} and a frequency value equal to 0.50 Hz. By comparing the results obtained, it was decided to use mesh B with 351,134 (shown in Fig. 4) elements because it represents a good compromise between the accuracy of the results and computational time.

The numerical model was then validated with experimental data

Table 2
Air temperature for three different meshes.

Mesh name	Cell Number	f (Hz)	u_0 (m/s)	$T_{out,air}$ (K)	$\%_{error}$	Computational average time (hour)
A	175,000	0.50	9.00	283.65	+0.90	3.5
B	**351,134**	**0.50**	**9.00**	**281.12**	+0.003	**5**
C	702,000	0.50	9.00	281.11	–	12.5

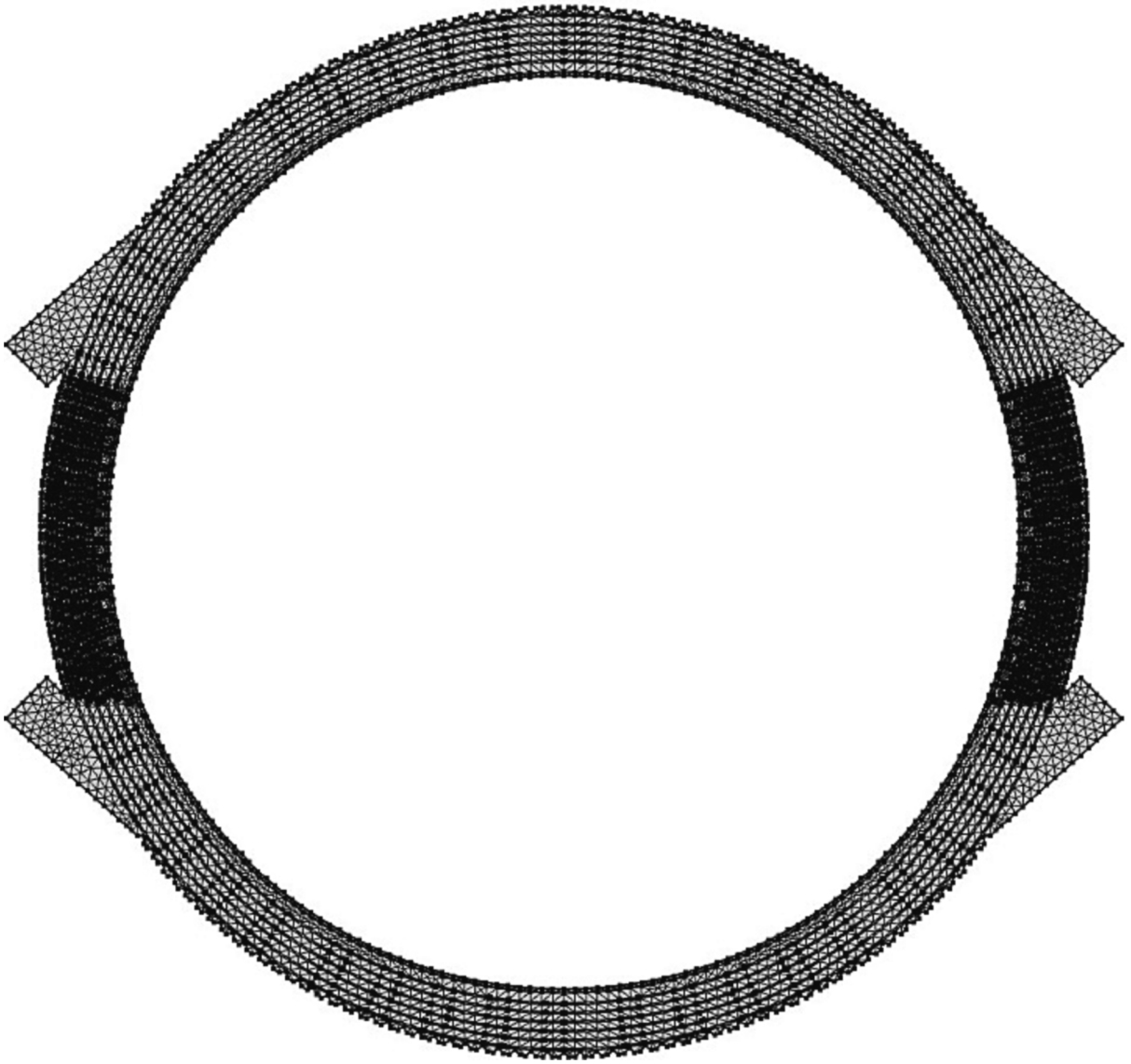

Fig. 4. Free triangular mesh of the 2-D rotary model.

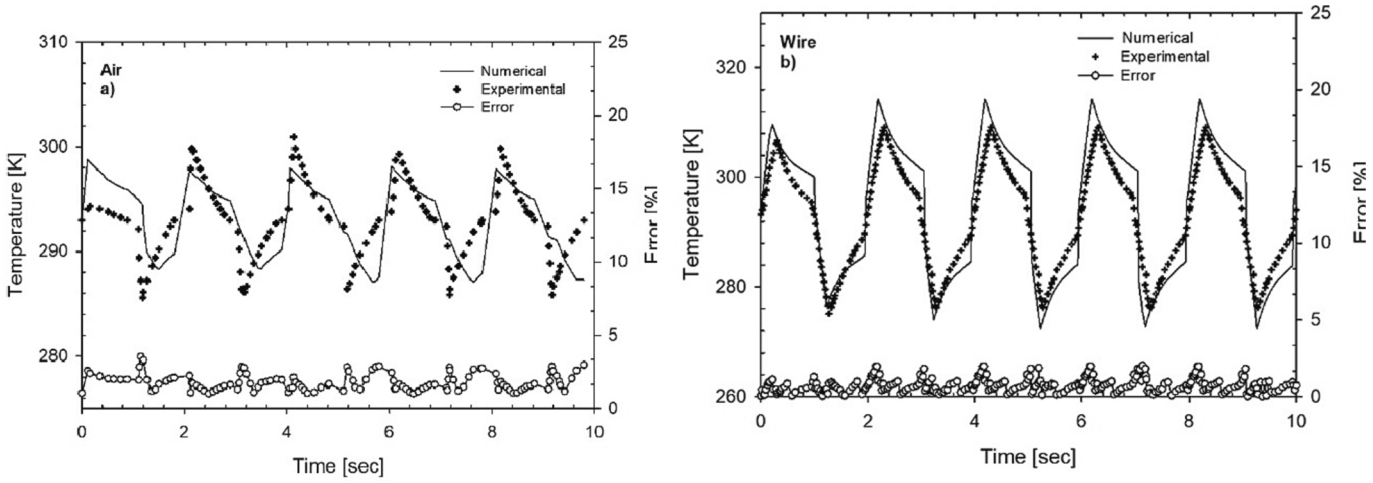

Fig. 5. A comparison between experimental [28] and numerical results in terms of temperature as a function of time: (a) the air; (b) a wire in the device.

from the rotary prototype developed at the Saarland University, which had a geometry similar to our device [28]. In this device, the wire loading and unloading process took place through the movement of the wires on the ramp of a specifically designed cam. The material used was a quaternary alloy $Ni_{45}Ti_{47.25}$ $Cu_5V_{2.75}$ with 240 wires of diameter 0.2 mm and length 300 mm (total mass 50 g) under a rotation frequency of 0.5 Hz. In the simulations, the air enters the device with a speed of 8 m s^{-1} and a temperature of 293 K. Simulations have been carried out through the 2D model using all the geometric and operational parameters indicated in the paper [28]. The comparison between the model

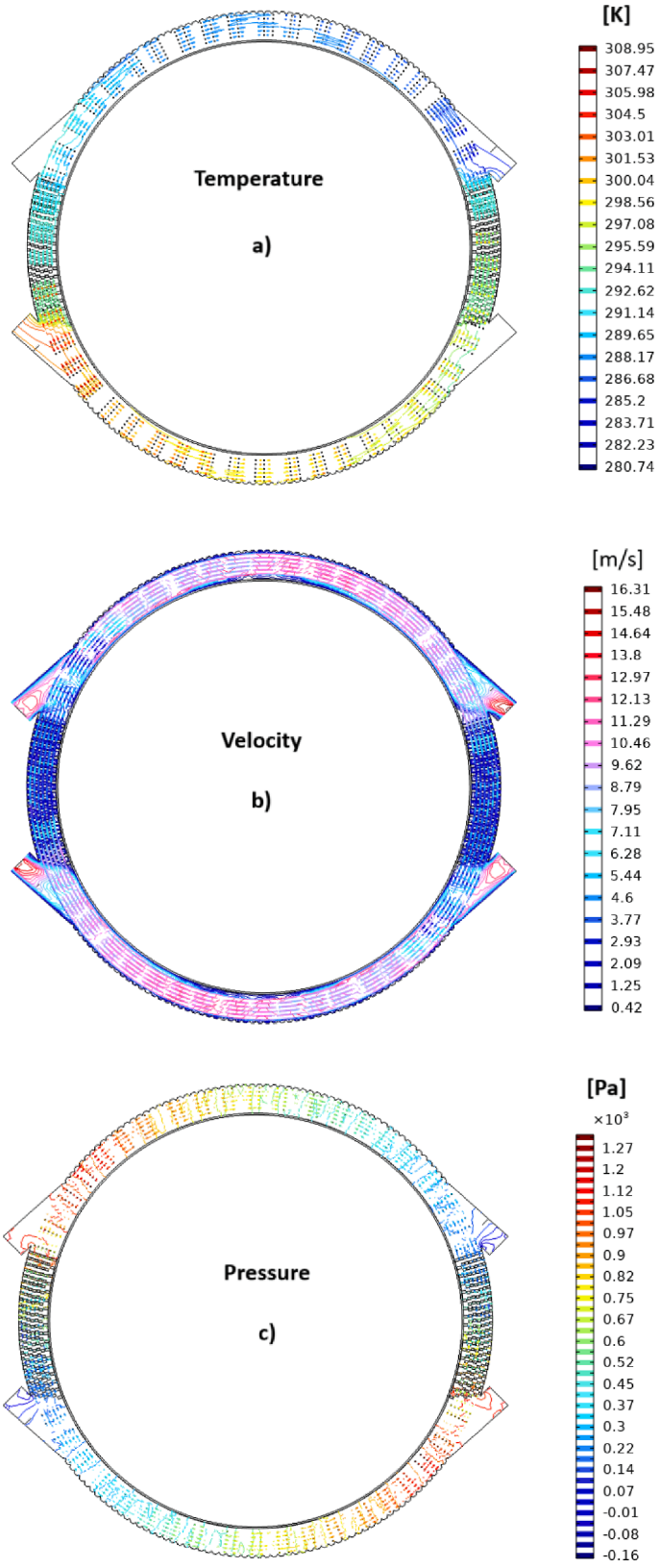

Fig. 6. 2D Contour maps at rotation frequency equal to 0.5 Hz, air velocity 12 m s^{-1} at instant 3.91 s: a) temperature; b) velocity; c) pressure.

and the experimental results has been reported in Fig. 5; besides, the researchers have shared the video consultable through the link reported in [40].

In particular, Fig. 5(a) shows the comparison in terms of the time trend of the temperature of the air leaving the cold regenerator of the device, whereas Fig. 5 (b) shows the temperature profiles in the wires of elastocaloric material during the four phases of the AeR cycle.

Two main factors dictate the difference between the numerical and experimental values: uncertainty of the measuring instruments and, in particular by the position of the temperature sensor; in fact, the authors of the experimental study position the probe exactly and at a given instant of time, while the numerical model defines the average temperature value at the channel outlet. Furthermore, the error curve is provided in both the comparison and it shows an acceptable fairness between numerical and experimental data (maximum deviancy 3.7% and 2.1% as regards the temperatures of the air and the elastocaloric material, respectively). Therefore, the model predicts the results in more than acceptable ways.

5. Results

Following the completion of the campaign on numerical investigation, the velocity, pressure, and temperature fields obtained from the simulation of the 2D rotating model are presented.

Fig. 6 presents the velocity (a), pressure (b), and temperature (c) contour map obtained for at a velocity of 12 m s^{-1} and a frequency of 0.5 Hz. Fig. 6(a) shows that the fluid velocity along the channel reaches a value of 9 m s^{-1}. This reduction compared to the inlet velocity of 12 m s^{-1} is partly attributed to the presence of the boundary layer on the wires and near the inner and outer crown and partly to the strong pressure gradient in the transition zone, resulting in a significant deceleration of the fluid in the immediate downstream region of the inlet channel. Fig. 6 (b) reveals that the pressure drop between the inlet and outlet of the flow is approximately 1000 Pa. Lastly, Fig. 6(c) depicts the temperature distribution inside the regenerator, highlighting a temperature variation of approximately 8 K for the air in both the hot and cold sides.

The Fig. 7 shows that the lowest air temperature (280 K) is reached at a frequency of 0.3 Hz with a velocity of 6 m s^{-1} corresponding to a ϕ^* of 0.44.

In Fig. 8 the air temperature variation in the cold regenerator vs the utilization factor, parametrized for cycle frequency is reported. The temperature variation for each frequency initially increases with velocity, then reaches a maximum, and finally decreases. Indeed, by increasing the velocity, the air convective heat transfer coefficient also increases. Therefore, an optimal fluid velocity corresponds to the point where air can utilize the entire energy available from the elastocaloric effect. Further air flow rate perturbs the temperature profile of the AeR, thus decreasing the temperature difference between the air and the wires. The latter quickly becomes overwhelmed by the fluid flow, and the heat transfer efficiency decreases.

As the frequency increases, the maximum point moves toward the right-side of the graph because the maximum power that can be subtracted increases proportionally and therefore a higher ϕ^* is needed.

The temperature variation increases with frequency in the high speeds zone and decreases for small ϕ^*. As the frequency varies, the fluid passage time also changes. Under low speeds, the ΔT_{COLD} is a decreasing function of the frequency: the heat exchange mechanism is not effective, and the fluid has more time to exchange heat with the wires. Under high speeds ΔT_{COLD} is an increasing function of the frequency. The heat exchange mechanism is effective; therefore, for a too large fluid passage time, the heat exchange process's driving force decreases with the heat exchange's effectiveness.

The greatest value of the air temperature variation detected is 12.3 K at 0.3 Hz and 0.44 as cycle frequency and utilization factor, respectively. A similar value (11.7 K) can also be obtained at 0.7 Hz for a utilization factor of 0.56.

In Fig. 9 the cooling power vs ϕ^* parametrized for cycle frequency is reported. It can be noted that the cooling power at high frequencies increases with ϕ^* because the fluid mass flow rate also increases. At low frequencies, it initially grows, then it touches a maximum, and finally, it falls due to the effect of decreasing ΔT_{COLD}. The variations of cooling power with frequency are less relevant in the low-ϕ^* area. In the high-ϕ^*-area, on the other hand, the increase in cooling power with frequency is more significant and it is due to the increase in ΔT.

The variation of the cooling power with frequency is less relevant in the low-ϕ^* zone. In the high-ϕ^* zone, on the other hand, the increase in

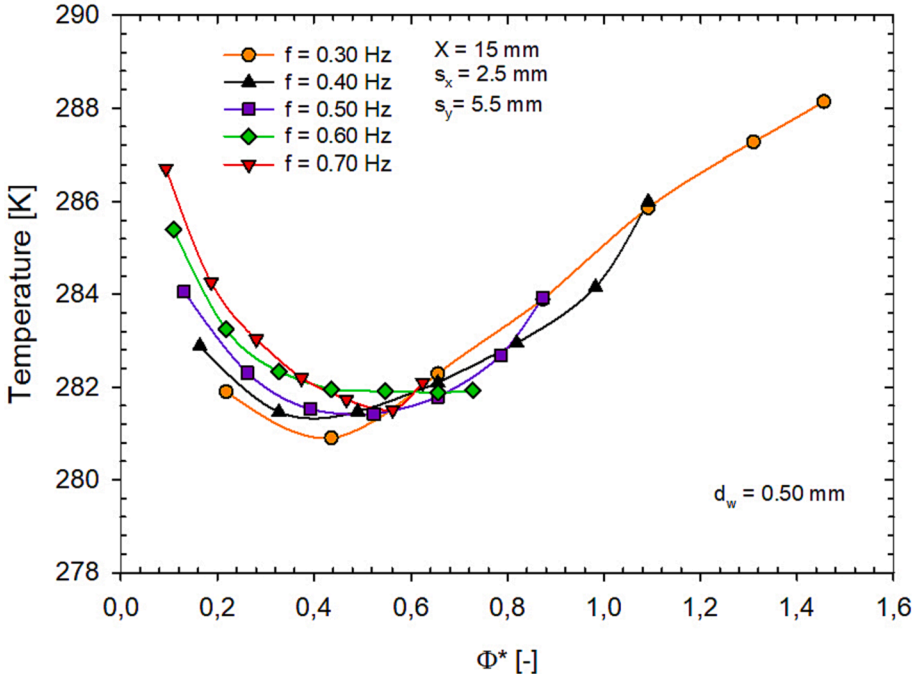

Fig. 7. Air temperature at the outlet of the cold regenerator as a function of the utilization factor for different cycle frequencies.

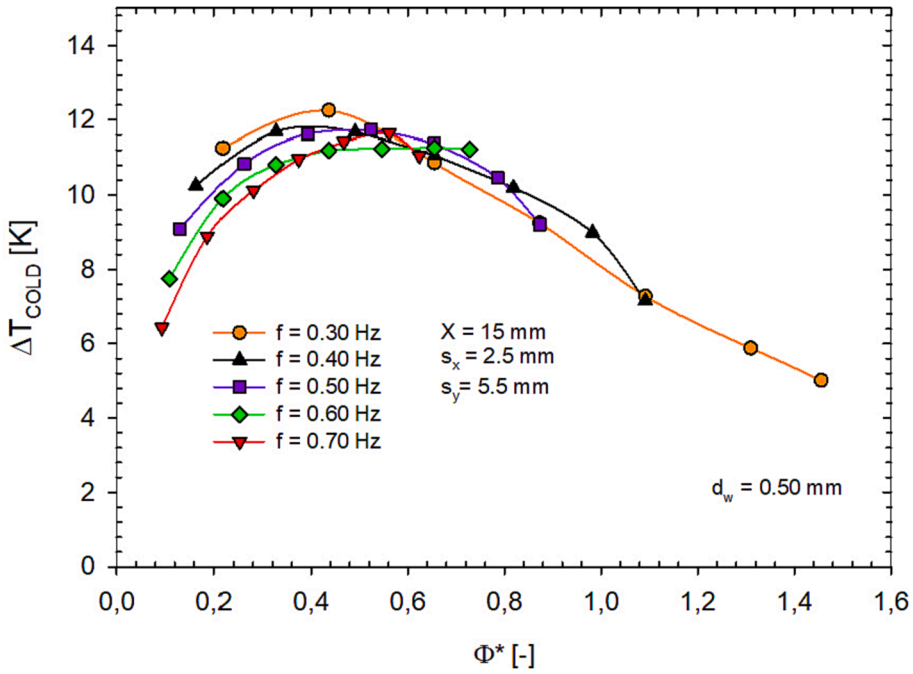

Fig. 8. Air temperature variation in the cold regenerator vs utilization facto parametrized for cycle frequencies.

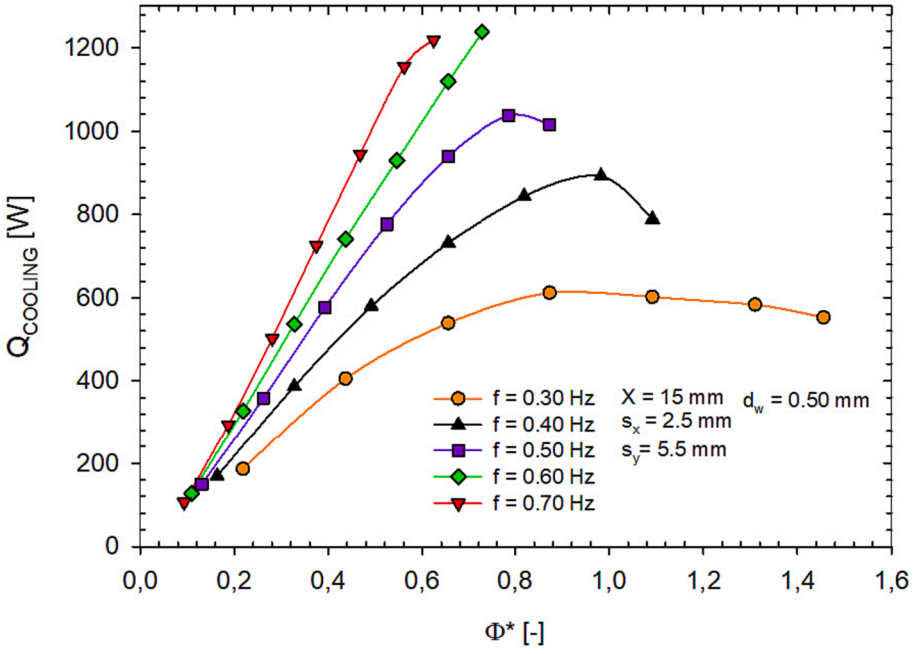

Fig. 9. Cooling power vs utilization factor parametrized for cycle frequency.

cooling power with frequency is more significant and is due to the increase in ΔT_{COLD}.

At high ϕ^*, very promising cooling power values are reached to be considered suitable for applications oriented to the macro-scale field (greater than 1000 W), with a maximum of 1240 W at 0.6 Hz and with a speed of 20 m s^{-1}(corresponding to a$\phi^* = 0.73$). This value is very encouraging because it corresponds to a Specific Cooling Power (SCP) of 5400 W kg^{-1}, higher than the ones carried out by the prototypes that have been designed up to now.

In Fig. 10 the temperature span vs utilization factor parametrized for the cycle frequency is plotted.

The temperature span of an elastocaloric device is determined by the specific material used and its thermomechanical properties. It is typically defined by the upper and lower temperature limits within which the device can effectively transfer heat and provide cooling. The Figure shows that the ΔT_{span} that can be obtained is always greater than 10 K, reaching the highest value of 28.5 K at a speed of 3 m s^{-1} and a frequency of 0.3 Hz, i.e. for$\phi^* = 0.22$.

The variation of the coefficient of performance with ϕ^* parametrized for the frequency is visible in Fig. 11. Additionally, in Fig. 12(a) and (b) the pressure drops and the pumping power as a function of the utilization factor are visible.

Fig. 11 clearly shows that there are two areas of the graph: one at low ϕ^* (corresponding to low air speeds, i.e. from 3 to 9 m s^{-1}), and one at

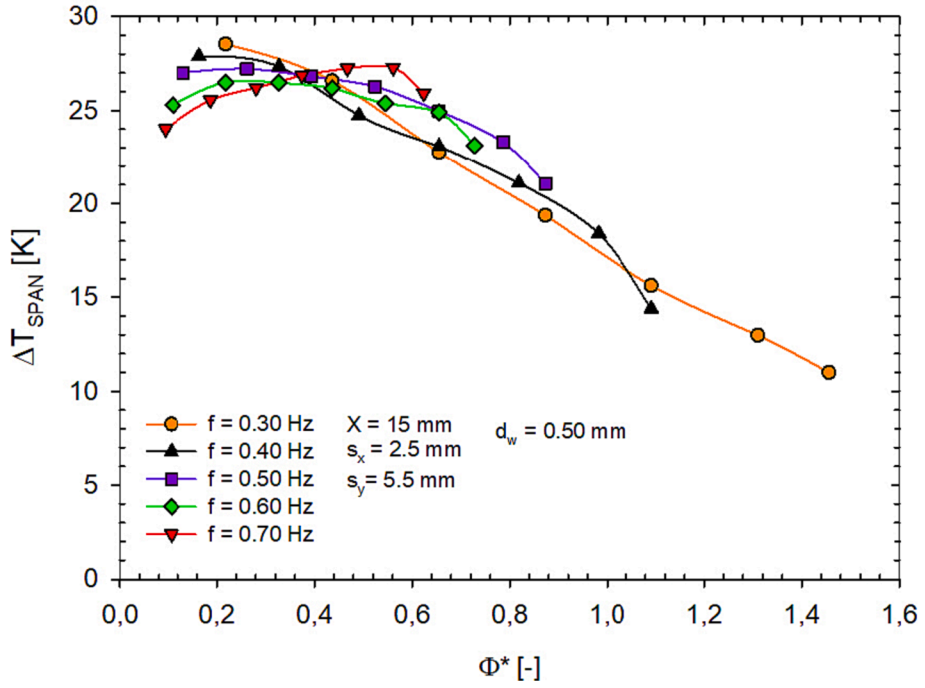

Fig. 10. Temperature span vs utilization factor parametrized for cycle frequency.

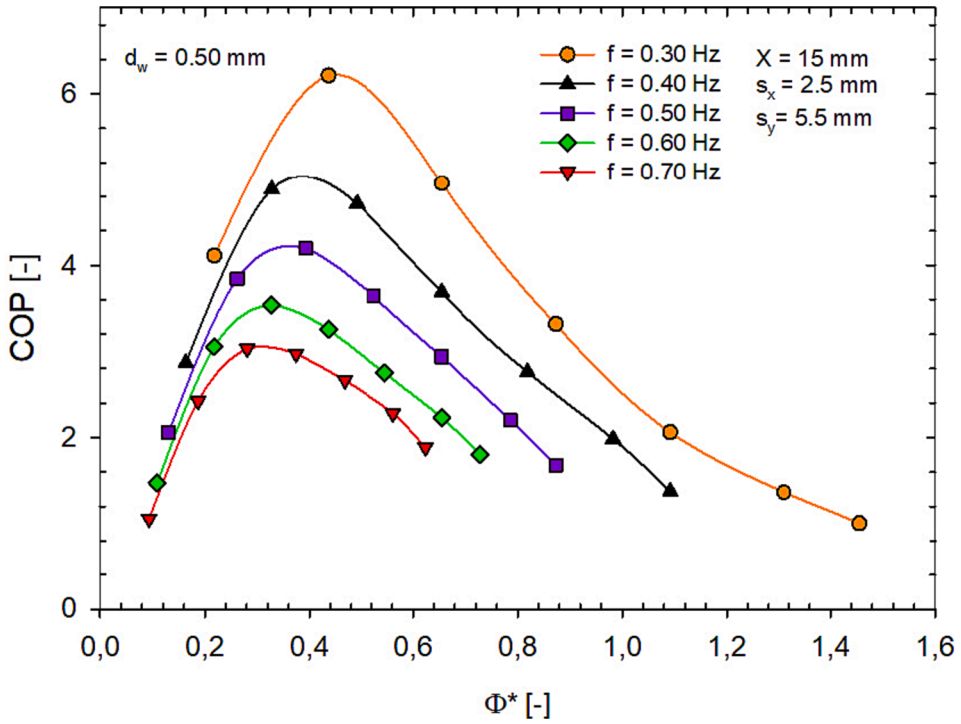

Fig. 11. COP. as a function of utilization factor for different cycle frequency values.

high ϕ^* (corresponding to high speeds, i.e. from 9 to 20 m s^{-1}). In the low-ϕ^* area, the COP increases as the frequency decreases. This trend is due to the higher temperature variation in the cold regenerator at low frequencies. In the high-ϕ^* area, the cold temperature variation at low frequencies decreases with the cooling power and, therefore, the COP for the same net-work.

For each frequency, however, the COP increases as the fluid velocity increases, reaches a maximum and decreases. The augmentation of the pressure drops (Fig. 12(a)) affects the values of COP at large velocities, thus, the power expenditure coupled with the work of the fan is also increased (Fig. 12(b)). Therefore, a fluid velocity greater than 9 m s^{-1} is not recommendable. It should also be noted that the maximum value of the COP corresponds to a higher speed as the cycle frequency increases. The maximum COP (6.22) is obtained at a $\phi^* = 0.44$ and a frequency of 0.3 Hz.

The second law efficiency is plotted vs the velocity of the heat transfer fluid parametrized for the considered frequencies in Fig. 13. The

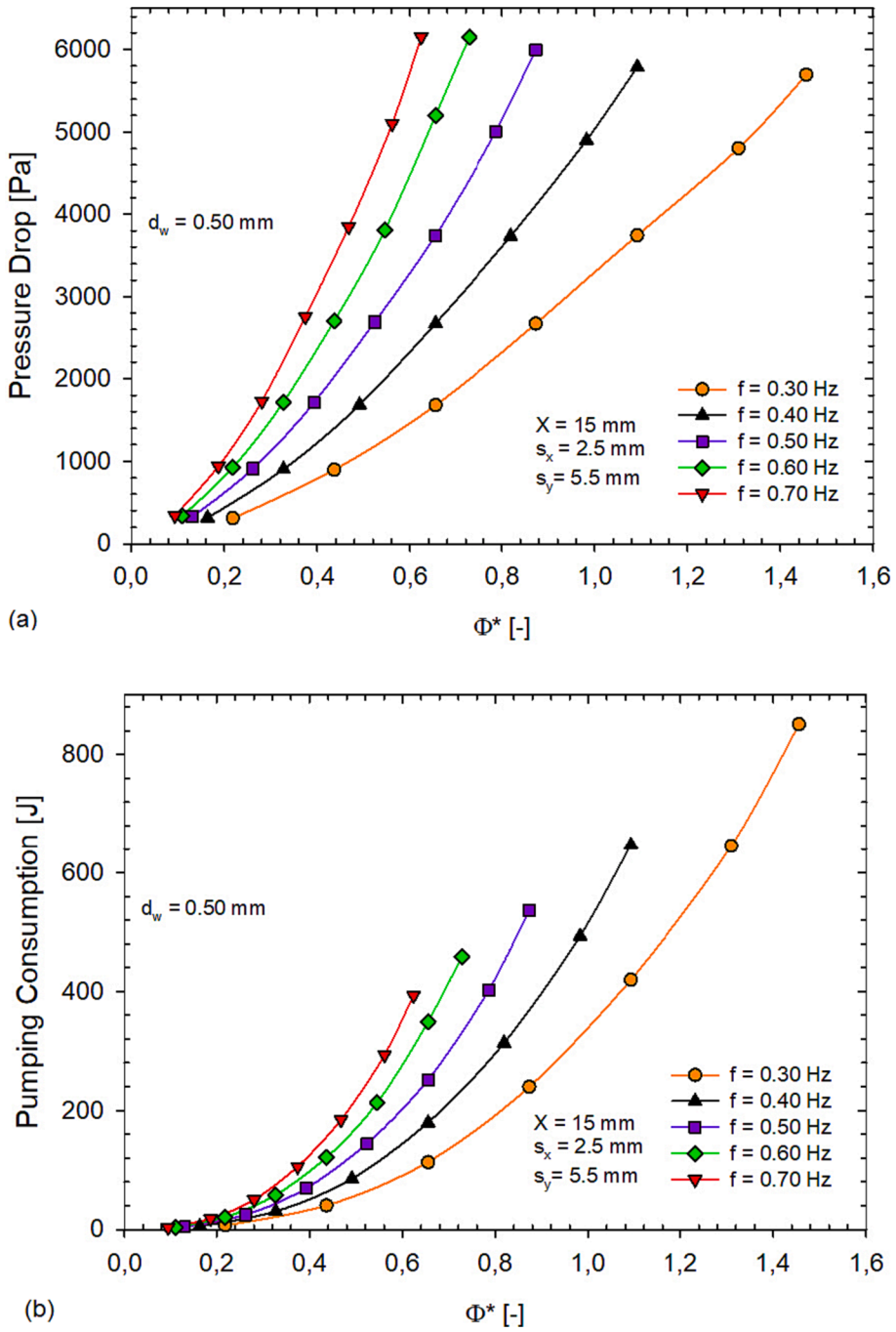

Fig. 12. (a)Pressure drop and (b) pumping power as a function of utilization factor for different values of cycle frequency.

results are very promising in the zone of low air velocity of the diagram up to a maximum of 60%.

6. Conclusions

As output of this paper, a map of energy performance by varying the operative conditions (air speed and cycle frequency) has been constructed to explore the potential of the prototype while operating in cooling mode. Based on the tests carried out, the following results can be highlighted:

- a maximum air temperature variation of 12.3 K has been obtained at a cycle frequency of 0.3 Hz and an air velocity of 6 m s^{-1} (corresponding to a utilization factor of 0.44).
- A maximum value of the temperature span of 28.5 K is achieved at a speed of 3 m s^{-1} and a frequency of 0.3 Hz (corresponding to $\phi^* = 0.22$)
- Cooling power values greater than 1000 W are reached at high speeds and frequencies.
- The maximum cooling power is a maximum of 1240 W at 0.6 Hz and with a speed of 20 m s^{-1}(corresponding to $a\phi^* = 0.73$ and to a Specific Cooling Power of 5400 W kg^{-1}).
- Acceptable Coefficient Of Performance values have been found for speed values up to of 9 m s^{-1}; over them, the contributions related to the work of the fan become too relevant.
- A maximum Coefficient Of Performance of 6.22 (corresponding to a second law analysis efficiency of 60%) has been achieved is obtained at a $\phi^* = 0.44$ and a frequency of 0.3 Hz..

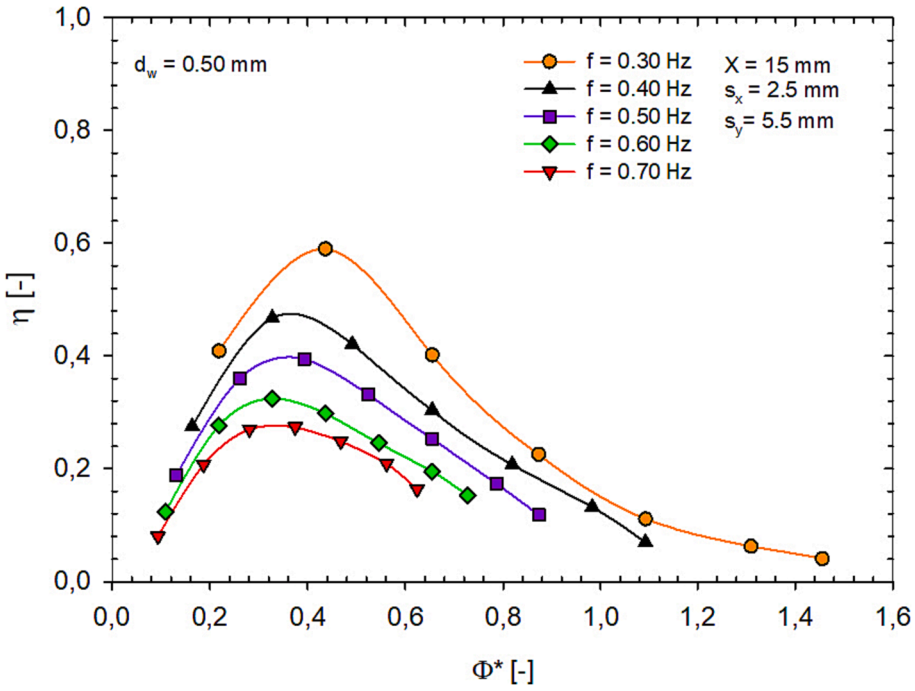

Fig. 13. Second law efficiency vs utilization factor parametrized for cycle frequency.

Indeed the values and trends of the calculated energy performances seem to be The results obtained show that the energy performances of the prototype are very positive for collocation of the device's intended use on the macroscale. Furthermore, to optimize the functioning of the device, it is advisable to operate with an air speed of 6 m s^{-1} and a frequency of 0.3 Hz, corresponding to $\phi^* = 0.44$.

Declaration of Competing Interest

The authors declare the following financial interests/personal relationships which may be considered as potential competing interests: Adriana Greco reports financial support was provided by Government of Italy Ministry of Education University and Research.

Data availability

Data will be made available on request.

Appendix A. Supplementary data

Supplementary data to this article can be found online at https://doi.org/10.1016/j.applthermaleng.2023.121517.

References

[1] Montreal Protocol on Substances that Deplete the Ozone Layer Final Act 1987." [Online]. Available: https://academic.oup.com/jel/article/1/1/128/673254.
[2] C. Aprea, A. Greco, A. Rosato, Comparison of R407C and R417A heat transfer coefficients and pressure drops during flow boiling in a horizontal smooth tube, Energ. Conver. Manage. 49 (6) (2008) 1629–1636.
[3] A. Greco, G.P. Vanoli, Evaporation of refrigerants in a smooth horizontal tube: Prediction of R22 and R507 heat transfer coefficients and pressure drop, Appl. Therm. Eng. 24 (14–15) (2004) 2189–2206.
[4] Kyoto Protocol to the United Nation Framework Convention on Climate Change, Kyoto, JPN, 1997.
[5] J.L.C. Fannou, C. Rousseau, L. Lamarche, S. Kajl, A comparative performance study of a direct expansion geothermal evaporator using R410A and R407C as refrigerant alternatives to R22, Appl. Therm. Eng. 82 (2015) 306–317.
[6] F. Molés, J. Navarro-Esbrí, B. Peris, A. Mota-Babiloni, Á. Barragán-Cervera, K. K. Kontomaris, Low GWP alternatives to HFC-245fa in Organic Rankine Cycles for low temperature heat recovery: HCFO-1233zd-E and HFO-1336mzz-Z, Appl. Therm. Eng. 71 (1) (2014) 204–212.
[7] C. Aprea, F. de Rossi, A. Greco, C. Renno, Refrigeration plant exergetic analysis varying the compressor capacity, Int. J. Energy Res. 27 (7) (2003) 653–669.
[8] C. Aprea, A. Greco, A. Maiorino, C. Masselli, The employment of caloric-effect materials for solid-state heat pumping, Int. J. Refrig. 109 (2020) 1–11.
[9] C. Aprea, A. Greco, A. Maiorino, C. Masselli, The use of barocaloric effect for energy saving in a domestic refrigerator with ethylene-glycol based nanofluids: A numerical analysis and a comparison with a vapor compression cooler, Energy 190 (2020), 116404.
[10] A. Kitanovski, P.W. Egolf, Innovative ideas for future research on magnetocaloric technologies, Int. J. Refrig. 33 (3) (2010) 449–464.
[11] P.V. Trevizoli, J.R. Barbosa Jr, A. Tura, D. Arnold, A. Rowe, Modeling of thermomagnetic phenomena in active magnetocaloric regenerators, J. Therm. Sci. Eng. Appl. 6 (3) (2014), 031016.
[12] C. Aprea, A. Greco, A. Maiorino, C. Masselli, A comparison between electrocaloric and magnetocaloric materials for solid state refrigeration, Int. J. Heat Technol. 35 (1) (2017) 225–234.
[13] U. Tomc, J. Tušek, A. Kitanovski, A. Poredoš, A new magnetocaloric refrigeration principle with solid-state thermoelectric thermal diodes, Appl. Therm. Eng. 58 (1–2) (2013) 1–10.
[14] W. de Vries, T.H. van der Meer, Application of Peltier thermal diodes in a magnetocaloric heat pump, Appl. Therm. Eng. 111 (2017) 377–386.
[15] T. Lei, K. Engelbrecht, K.K. Nielsen, C.T. Veje, Study of geometries of active magnetic regenerators for room temperature magnetocaloric refrigeration, Appl. Therm. Eng. 111 (2017) 1232–1243.
[16] A. Greco, C. Aprea, A. Maiorino, C. Masselli, A review of the state of the art of solid-state caloric cooling processes at room-temperature before 2019, Int. J. Refrig 106 (2019) 66–88.
[17] A. Czernuszewicz, L. Griffith, A. Scott, J. Slaughter, V. Pecharsky, Unlocking large compressive strains in thin active elastocaloric layers, Appl. Therm. Eng. 190 (2021), 116850.
[18] S. Qian, Thermodynamics of elastocaloric cooling and heat pump cycles, Appl. Therm. Eng. 219 (2023), 119540.
[19] L. Cirillo, A. Greco, C. Masselli, Development of an electronic circuit cooling system using elastocaloric effect: a FEM comparison among different configurations, Appl. Therm. Eng. 219 (2023), 119463.
[20] L. Yuan, Y. Wang, J. Yu, A. Greco, C. Masselli, S. Qian, Numerical study of a double-effect elastocaloric cooling system powered by low-grade heat, Appl. Therm. Eng. 218 (2023), 119302.
[21] Y. Chen, Y. Wang, W. Sun, J. Liu, S. Qian, A compact elastocaloric refrigerator, Innov. 3 (2022), 100205.
[22] Saylor, A., 2012. ARPA-E summit technology showcase. http://www.energy.gov/articles/2012-arpa-e-summittechnology-showcase (Retrieved on Nov. 12, 2015).
[23] S. Qian, Y. Wu, J. Ling, J. Muehlbauer, Y. Hwang, I. Takeuchi, R. Radermacher, Design, development and testing of a compressive thermoelastic cooling prototype. Proceedings of 24th IIR International congress of refrigeration ICR 2015, 2015.
[24] S. Qian, A. Alabdulkarem, J. Ling, J. Muehlbauer, Y. Hwang, R. Radermacher, I. Takeuchi, Performance enhancement of a compressive thermoelastic cooling system using multi-objective optimization and novel designs, Int. J. Refrig 57 (2015) 62–76.

[25] S. Qian, Y. Geng, Y. Wang, J. Muehlbauer, J. Ling, Y. Hwang, I. Takeuchi, Design of a hydraulically driven compressive elastocaloric cooling system, Sci. Technol. Built Environ. 22 (5) (2016) 500–506.
[26] J. Tušek, K. Engelbrecht, D. Eriksen, S. Dall'Olio, J. Tušek, N. Pryds, A regenerative elastocaloric heat pump, Nat. Energy 1 (10) (2016) 1–6.
[27] K. Engelbrecht, J. Tušek, D. Eriksen, T. Lei, C.Y. Lee, J. Tušek, N. Pryds, A regenerative elastocaloric device: experimental results, J. Phys. D Appl. Phys. 50 (42) (2017), 424006.
[28] S.M. Kirsch, F. Welsch, N. Michaelis, M. Schmidt, A. Wieczorek, J. Frenzel, S. Seelecke, NiTi-Based Elastocaloric Cooling on the Macroscale: From Basic Concepts to Realization, Energ. Technol. 6 (8) (2018) 1567–1587.
[29] X. Li, S. Cheng, Q. Sun, A compact NiTi elastocaloric air cooler with low force bending actuation, Appl. Thermal Eng. 215 (October 2022) (2022), 118942.
[30] L. Ianniciello, K. Bartholomé, A. Fitger, K. Engelbrecht, Long life elastocaloric regenerator operating under compression, Appl. Therm. Eng. 202 (2022), 117838.
[31] Z. Ahcin, S. Dall'Olio, A. Zerovnik, U.Z. Baskovic, L. Porenta, P. Kabirifar, J. Cerar, M. Zupan, J. Klemenc, J. Tusek, High-performance cooling and heat pumping beased on fatigue-resistent elastocaloric effect in compression, Joule 6 (2022) 2338–2357.
[32] S. Qian, D. Catalini, J. Muehlbauer, B. Liu, H. Mevada, H. Hou, I. Takeuchi, High-performance multimode elastocaloric cooling system, Science 380 (6646) (2023) 722–727.
[33] S. Qian, J. Ling, Y. Hwang, R. Radermacher, I. Takeuchi, Thermodynamics cycle analysis and numerical modeling of thermoelastic cooling systems, Int. J. Refrig 56 (2015) 65–80.
[34] J. Tušek, K. Engelbrecht, N. Pryds, Elastocaloric effect of a Ni-Ti plate to be applied in a regenerator-based cooling device, Sci. Technol. Built Environ. 22 (5) (2016) 489–499.
[35] Z. Ahčin, P. Kabirifar, L. Porenta, M. Brojan, J. Tušek, Numerical Modeling of Shell-and-Tube-like Elastocaloric Regenerator, Energies (Basel) 15 (23) (2022).
[36] D.J. Silva, J. Ventura, J.P. Araújo, Caloric devices: A review on numerical modeling and optimization strategies. *International Journal of Energy Research*, vol. 45, no. 13. John Wiley and Sons Ltd, pp. 18498–18539, 2021.
[37] L. Cirillo, A. Rosaria Farina, A. Greco, C. Masselli, The optimization of the energy performances of a single bunch of elastocaloric elements to be employed in an experimental device, Thermal Sci. Eng. Progr. 27 (2022), 101152.
[38] O. Heintze, S. Seelecke, A coupled thermomechanical model for shape memory alloys-From single crystal to polycrystal, Mater. Sci. Eng. A 481–482 (1–2 C) (2008) 389–394.
[39] S. Whitaker, Forced convection heat transfer calculation for flow in pipes, past flat plates, single cyclinders and for flow in packed beds and tube bundles, AIChE J. 18 (1972) 361–371.
[40] https://www.youtube.com/watch?v=eP6JD5OKroI&t=5s.